IMA Journal of Applied Mathematics (2019) **84**, 854–872
doi:10.1093/imamat/hxz018
Advance Access publication on 26 September 2019

Centre modes in pipe flow

Ozge Ozcakir* and Philip Hall
School of Mathematics, Monash University, Clayton, VIC 3800, Australia
*Corresponding author: ozge.ozcakir@monash.edu

and

Saleh Tanveer
Department of Mathematics, The Ohio State University, Columbus, OH 43210, USA

[Received on 13 November 2018; revised on 24 May 2019; accepted on 14 July 2019]

In two previous papers, Ozcakir, Tanveer, Hall, & Overman (2016, Travelling waves in pipe flow, *J. Fluid Mech.*, **791**, 284–328) and Ozcakir, Hall & Tanveer (2019, Nonlinear exact coherent structures in pipe flow and their instabilities, *J. Fluid Mech.*, **868**, 341–368) investigated numerically and asymptotically high Reynolds number exact coherent structures in pipe flow. It was found that, in addition to the structures described by the vortex–wave interaction theory by Hall & Smith (1991, On strongly nonlinear vortex/wave interactions in boundary layer transition. *J. Fluid Mech.*, **227**, 641–666), there exists vortical structures localized near the centre of the pipe with a core of size $O(Re^{-1/4})$ convected downstream at a speed that deviates from the pipe centreline speed by $O(Re^{-1/2})$, where Re is the Reynolds number. In the finite Reynolds number calculations by Ozcakir, Tanveer, Hall & Overman (2016, Travelling waves in pipe flow, *J. Fluid Mech.*, **791**, 284–328), asymptotic state was referred to as a nonlinear viscous core state (NVC). However the reduced asymptotic equations were not solved and only limited confirmation of the theory was found numerically. Here, in order to conclusively confirm the existence of the NVC state we first describe direct numerical calculations on the asymptotically reduced $Re >> 1$ equations for such state states. The results are then compared in detail to the finite Re calculations up-to $Re = 10^6$; the latter regime is at much higher values of the Reynolds number than those reported in Ozcakir, Tanveer, Hall & Overman (2016, Travelling waves in pipe flow, *J. Fluid Mech.*, **791**, 284–328). The results are found to be in excellent agreement with the finite Re calculations in a region between $Re = 10^5$ and 10^6, thereby confirming that the structure observed by Ozcakir, Tanveer, Hall & Overman (2016, Travelling waves in pipe flow, *J. Fluid Mech.*, **791**, 284–328) is indeed a finite Reynolds number realization of an asymptotic NVC state.

Keywords: pipe flows; turbulence.

1. Introduction

Research on exact coherent structures in shear flows has been a topic of much recent interest. Most of the work done in this area has been limited to fully numerical investigation of nonlinear equilibrium solutions in different geometries. However it is believed that for moderate to large Reynolds number Re, they correspond to coherent states in a turbulent flow that are observable experimentally if the unstable manifolds of these states are sufficiently low-dimensional and their evolution in time is slow. Indeed, in intermediate Reynolds number turbulence, it has been observed in the experiments of Hof *et al.* (2004) that the flow migrates between different travelling wave states.

Most of these coherent states at finite Reynolds number have been found through numerical computations in channels by Nagata (1990), Waleffe (2001), Waleffe (2003), Wang *et al.* (2007), Gibson *et al.* (2009) and Blackburn *et al.* (2013) and in pipe flows by Faisst & Eckhardt (2003), Wedin & Kerswell (2004), Kerswell (2007), Viswanath (2007) and Willis *et al.* (2017) with different degrees of symmetry. The physical mechanism to sustain such steady states for large Reynolds number is now well-understood and is precisely the vortex–wave interaction scenario discussed by Hall & Smith (1991), henceforth we will refer to that interaction as VWI. However, the efficient and accurate numerical solution of the three-dimensional large Reynolds number travelling wave solutions of the Navier–Stokes equations is challenging since both the wall boundary layer and internal critical layers have to be adequately resolved. This requires a large number of modes in the radial direction, which leads to a large matrix inversion problem for the associated Newton iteration scheme.

There have been a small number of developments in the asymptotic theory for these states as $Re \to \infty$ that shed light on the physical mechanisms involved and confirm the numerically observed trends. However the numerical calculations cannot be continued indefinitely for large Re due to computational limitations as the length scale of the structures shrinks asymptotically to zero. While investigating boundary layers for large Re, Hall & Smith (1991) realized that in any shear flow, small $O\left(\frac{1}{Re}\right)$ roll components drive an $O(1)$ streaky flow that can support neutral inviscid modes in the form of travelling waves. The Reynolds stress term arising from the streamwise average of the quadratic terms involving the waves drives the rolls. Subsequently Hall & Sherwin (2010) used the framework given by Hall & Smith (1991) in a channel flow to determine solutions of the parameter free equations to confirm that the VWI asymptotic state is the high Reynolds number description of what had become to be known in the computational community as a *self-sustaining process* (SSP); see for example Waleffe (1995). The calculations of Hall & Sherwin (2010) and Deguchi & Hall (2014a) show remarkable agreement between the finite Reynolds number computations of lower-branch modes and the asymptotic VWI approach even at low Reynolds numbers. Although the upper-branch modes calculated at large but finite Re approach the asymptotic state much more slowly, nonetheless they are still described by the VWI theory.

Using scaling arguments Ozcakir *et al.* (2016) have investigated the possible large Re asymptotic structures involving travelling waves in a pipe when the axial wave number α is $O(1)$ and presented general asymptotic arguments for $Re \to \infty$ that identify two possible classes of solutions. The first is a class of VWI states, which further breaks up into two sub-classes with a core radius width scaling as $\delta = 1$ or $\delta = Re^{-1/6}$ depending on whether or not the vortex wave-structure shrinks towards the pipe centre. For a VWI solution, small linear waves of amplitude $O(Re^{-5/6}\delta^{-4/3})$ concentrated mostly in a critical layer of width $\delta(Re\delta^4)^{-1/3}$ drive rolls of magnitude $O(Re^{-1}\delta^{-1/3})$ that generate streaks of magnitude δ^2, this three-way interaction is the basis of VWI theory derived formally in the high Reynolds number limit. In the SSP framework the same conclusion was reached by interrogating the numerical data from full Navier–Stokes solutions.

When $\delta = 1$, the scalings of this vortex wave solutions match those of Hall & Sherwin (2010) for VWI theory in plane Couette flow, and a comparison with the so-called S-anti-symmetric numerical solution of Viswanath (2009) shows that the latter is a finite Re realization of the VWI states. The detailed qualitative analysis of Ozcakir *et al.* (2019) suggests that the same is true for the Wedin & Kerswell (2004) solutions.

A second possibility is a class of nonlinear viscous core states, henceforth we refer to these as NVC states. These states have a quite different asymptotic structures than VWI states, with a core radius of size $\delta = Re^{-1/4}$, and the radial, azimuthal and axial velocity components scale as $Re^{-3/4}$, $Re^{-3/4}$

and $Re^{-1/2}$, respectively. This NVC state is similar in many respects to the free-stream coherent states discovered by Deguchi & Hall (2014b) in boundary layer flows. While the wave and roll components are localized in the shrinking core with algebraic decay as one moves away from the core, the streak component, though small, is the same size inside and outside the core, until the wall is approached. Unlike the boundary layer flows considered by Deguchi & Hall (2014b), there is no exponential growth of the streak away from the core; instead, the azimuthal component of the streak remains constant. These states are different from the helical centre modes of Smith & Bodonyi (1982), which were confirmed for finite R by Deguchi & Walton (2013) where the dependence in θ and z are linked. Furthermore, for the NVC states the axial wave and streak amplitude are of the same order throughout a shrinking core unlike the asymptotic states of Smith *et al.* (1990) where there is a critical layer shrinking towards pipe centre.

Based on the available numerical data in the range $Re \leqslant 1.3 \times 10^5$, Ozcakir *et al.* (2016) tentatively suggested that C1 and C2, the two branches found, were finite Re realizations of the asymptotically derived NVC states, even though, the agreement with the $Re \to \infty$ asymptotic theory was not as good for certain quantities as others. This discrepancy was attributed to finite Re effects. More recently Ozcakir *et al.* (2019), among other results, also reported numerical calculations of the $C1$ and $C2$ states at much higher values of $Re \sim 10^6$. The calculations suggested the $C1$-state arises as a shift-and-rotate symmetry breaking bifurcation from the $C2$ state, with only the $C2$ solution existing in the $Re \to \infty$ asymptotic limit.

While the work by Ozcakir *et al.* (2016) and Ozcakir *et al.* (2019) suggest that the scalings for NVC states are consistent with finite but large Reynolds number calculations there have been no direct solutions of the Reynolds number free equations describing NVC states. The aim of the present paper is to compute directly the canonical NVC states numerically based on the reduced $Re = \infty$ asymptotic equations and compare them to the full Navier–Stokes calculations of travelling waves at finite Re.

The outline of the paper is as follows: in section § 2 we briefly summarize the canonical parameter free problem for the NVC states. In section § 3 we provide details of our numerical approach. We follow this in section § 4 with a discussion of our results. Finally in section § 5, we draw some conclusions.

2. The canonical parameter free problem for NVC states

2.1 *Nonlinear eigenvalue problem*

In the context of pipe flow, we use cylindrical coordinates (r, θ, z) with the cylinder axis aligned along the z-axis. We non-dimensionalize all quantities of interest using the pipe radius and centreline velocity of the corresponding base flow and define the Reynolds number accordingly based on these length and velocity scales. The travelling wave solutions we are looking for satisfy the dimensionless Navier–Stokes equations

$$\mathbf{u}_t + \mathbf{u} \cdot \nabla \mathbf{u} = -\nabla p + \frac{1}{Re} \Delta \mathbf{u}, \nabla \cdot \mathbf{u} = 0, \tag{2.1}$$

where

$$\mathbf{u} = \mathbf{v}_B(r, \theta) + \mathbf{v}\,(r, \theta, z - ct)\,, \quad p = p_B(r, \theta) + \tilde{p}\,(r, \theta, z - ct)\,, \tag{2.2}$$

where $(\mathbf{v}_B, p_B) = ((1 - r^2)\hat{\mathbf{z}}, -\frac{4}{Re} z)$. We assume that the perturbation velocity $\mathbf{v}$ and the pressure $\tilde{p}$ are 2π periodic in θ, $2\pi/\alpha$ periodic in $\tilde{z} := z - ct$ and satisfy the no-slip boundary condition on the wall $r = 1$. The flow is driven by a constant mean axial pressure gradient $-(4/Re)\hat{z}$. It should be noted that

the axial transformation $\tilde{z} := z - ct$ implies $\frac{\partial}{\partial t} = -c\frac{\partial}{\partial \tilde{z}}$ and $\frac{\partial}{\partial z} = \frac{\partial}{\partial \tilde{z}}$. Therefore, it is appropriate to write $\frac{\partial}{\partial t}$ and $\frac{\partial}{\partial z}$ in terms of $\frac{\partial}{\partial \tilde{z}}$ hereafter.

On subtracting out Poiseuille flow and decomposing the remaining velocity into its axial component and its complement as $\mathbf{v} = \tilde{w}\hat{\mathbf{z}} + \mathbf{v}_\perp$, the Navier–Stokes equation for the perturbation velocity $\mathbf{v}$ and the corresponding pressure $\tilde{p}$ can be written in the form

$$\left(1 - c - r^2 + \tilde{w}\right)\partial_{\tilde{z}}\mathbf{v} + \left(\mathbf{v}_\perp \cdot \nabla_\perp\right)\mathbf{v} - 2r\left(\mathbf{v}\cdot\hat{\mathbf{r}}\right)\hat{\mathbf{z}} = -\nabla_\perp \tilde{p} - \frac{\partial \tilde{p}}{\partial \tilde{z}}\hat{\mathbf{z}} + Re^{-1}\Delta_\perp \mathbf{v} + Re^{-1}\frac{\partial^2}{\partial \tilde{z}^2}\mathbf{v} \quad (2.3)$$

$$\nabla_\perp \cdot \mathbf{v}_\perp + \frac{\partial \tilde{w}}{\partial \tilde{z}} = 0 \quad (2.4)$$

where $\nabla_\perp$ is the two-dimensional gradient operator defined in the (r, θ) plane.

Assuming we have a structure at the centre of the pipe of width $\delta \leqslant 1$ we introduce the stretched radial variable $\hat{r} = r/\delta$. The detailed consistency arguments by Ozcakir *et al.* (2016) suggest the existence of a travelling wave solution to (3) and (2.4) only when $\delta = 1, \delta = Re^{-1/6}$ and $\delta = Re^{-1/4}$. The first two cases are classified as VWI states and will not be discussed here.

When $\delta = Re^{-1/4}$, a completely coupled system of roll, streak and wave equations arise with the following form for the wave speed and scaled velocity and pressure fields

$$1 - c = Re^{-1/2}c_1 \quad \mathbf{v} = \tilde{w}\hat{\mathbf{z}} + \mathbf{v}_\perp \quad (2.5)$$

$$\tilde{w} = Re^{-1/2}\hat{w} \quad \mathbf{v}_\perp = Re^{-3/4}\hat{\mathbf{v}}_\perp \quad \text{and} \quad \tilde{p} = Re^{-3/2}\hat{p}. \quad (2.6)$$

Equations (2.3) and (2.4) then become

$$\left(c_1 - \hat{r}^2 + \hat{w}\right)\partial_{\tilde{z}}\hat{\mathbf{v}}_\perp + \hat{\mathbf{v}}_\perp \cdot \nabla_\perp \hat{\mathbf{v}}_\perp = -\nabla_\perp \hat{p} + \Delta_\perp \hat{\mathbf{v}}_\perp + \delta^2 \partial_{\tilde{z}}^2 \hat{\mathbf{v}}_\perp \quad (2.7)$$

$$\left(c_1 - \hat{r}^2 + \hat{w}\right)\partial_{\tilde{z}}\hat{w} + \hat{\mathbf{v}}_\perp \cdot \nabla_\perp \left(c_1 - \hat{r}^2 + \hat{w}\right) = -\delta^2 \partial_{\tilde{z}}\hat{p} + \Delta_\perp \hat{w} + \delta^2 \partial_{\tilde{z}}^2 \hat{w} \quad (2.8)$$

$$\nabla_\perp \cdot \hat{\mathbf{v}}_\perp + \frac{\partial \hat{w}}{\partial \tilde{z}} = 0 \quad (2.9)$$

in the $(\hat{r}, \theta, \tilde{z})$ domain.

To the leading order, $\delta^2 = O(Re^{-1/2})$ and thus it might appear all terms involving δ should be ignored. However, the streamwise momentum equation (2.8) along with (2.9) implies

$$\frac{d}{d\tilde{z}}\left\{\int_0^{2\pi}\int_0^{\infty}\left(c_1 - \hat{r}^2 + \hat{w}\right)\hat{w}\hat{r}\mathrm{d}\hat{r}\mathrm{d}\theta\right\} = -\delta^2\partial_{\tilde{z}}\left\{\int_0^{2\pi}\int_0^{\infty}\hat{p}\hat{r}\mathrm{d}\hat{r}\mathrm{d}\theta\right\}$$

As $\delta \to 0$, there is no reason for the left hand side to be zero; thus we have to account for the singular limit $\delta^2\partial_{\tilde{z}}\hat{p} \to H'(\tilde{z})$ as $\delta \to 0$ for some periodic function $H(\tilde{z})$. This leads to the following fully

nonlinear parameter-free eigenvalue problem in the infinite domain $0 < \hat{r} < \infty$, 2π-periodic in both θ and $\alpha\tilde{z}$ describing the limiting NVC states in a pipe:

$$\left(c_1 - \hat{r}^2 + \hat{w}\right) \partial_{\tilde{z}} \hat{\mathbf{v}}_\perp + \hat{\mathbf{v}}_\perp \cdot \nabla_\perp \hat{\mathbf{v}}_\perp = -\nabla_\perp \hat{p} + \Delta_\perp \hat{\mathbf{v}}_\perp, \tag{2.10}$$

$$\left(c_1 - \hat{r}^2 + \hat{w}\right) \partial_{\tilde{z}} \hat{w} + \hat{\mathbf{v}}_\perp \cdot \nabla_\perp \left(c_1 - \hat{r}^2 + \hat{w}\right) = -H'(\tilde{z}) + \Delta_\perp \hat{w}. \tag{2.11}$$

Equations (2.10) and (2.11) together with (2.9) are qualitatively analogous to a problem in boundary layer flow studied by Deguchi & Hall (2014b). In the shrinking core, the inner equation is a fully nonlinear eigenvalue problem with c_1 as the eigenvalue; the equations constitute a fully nonlinear Navier–Stokes problem with $Re = 1$. Solutions to this canonical equation only describe the flow structure inside the core at the centre of the pipe. They have to be supplemented by far-field matching conditions implied by the asymptotic solution outside the core, these will be explained in the next section; see equations (2.14), (2.15), (2.19) and (2.20).

2.2 *Far-field matching conditions under shift-and-rotate symmetry*

For the problem in scaled variables, the no-slip conditions are replaced by the far-field conditions on different azimuthal Fourier components. These are readily deduced from the discussions in Ozcakir *et al.* (2016) for all two-fold azimuthal symmetric flows. We refer the reader to Ozcakir *et al.* (2016) for a detailed derivation of the far-field conditions.

We introduce the new variables

$$\hat{\mathbf{v}}_\perp = \mathbf{U}(\hat{r}, \theta) + \mathbf{u}(\hat{r}, \theta, \tilde{z}) \quad \hat{w} = W(\hat{r}, \theta) + w(\hat{r}, \theta, \tilde{z}) \tag{2.12}$$

where $\mathbf{U}$ and W are referred to as the scaled roll and streak respectively, while $(\mathbf{u}, w)$ represent the scaled wave components with the axial wavelength average $\langle(\mathbf{u}, w)\rangle = 0$. On taking the axial wavelength average $\langle\cdot\rangle$ of (2.3) and (2.4), the projection of the velocity in the plane orthogonal to z-axis gives the roll equation. Since we limit our attention to $C2$ solutions with rotate-and-reflect symmetry, four-fold azimuthal symmetric rolls and streaks can be written as

$$\begin{pmatrix} U(\hat{r}, \theta) \\ V(\hat{r}, \theta) \\ W(\hat{r}, \theta) \end{pmatrix} = \sum_{k=0}^{\infty} \begin{pmatrix} U_{4k}(\hat{r}) \cos 4k\theta \\ V_{4k}(\hat{r}) \sin 4k\theta \\ W_{4k}(\hat{r}) \cos 4k\theta \end{pmatrix}. \tag{2.13}$$

An analysis of the roll equation derived from (2.10), which is discussed in the Appendix of Ozcakir *et al.* (2016), at leading order gives rise to the far-field conditions

$$U_{4k}, V_{4k} \sim \hat{r}^{-2k-1} \quad \text{for } k \geqslant 1, \tag{2.14}$$

so that

$$W_0 \sim \hat{r}^{-2}, \quad W_{4k} \sim \hat{r}^{-2k+2} \quad \text{for } k \geqslant 1. \tag{2.15}$$

In the above, for the sake of brevity, in using the symbol $\sim$, we deviate from the usual notation by omitting constants, i.e. $W_0 \sim \hat{r}^{-2}$ means $W_0 = C_0 \hat{r}^{-2} + o\left(\hat{r}^{-2}\right)$ for some constant C_0. Note that the

above asymptotic behaviour implies that the $\hat{r} >> 1$ behaviour of W is dominated by the $k = 1$ mode, and therefore $W(\hat{r}, \theta) \sim W_4(\hat{r}) \cos(4\theta) \sim \cos(4\theta)$.

On the other hand, subtracting the axially averaged equation (2.7) and (2.8) from (2.7) and (2.8) gives equations for the waves from which the equation for the pressure can be reduced to

$$\partial_{\hat{r}}^2 p_{kl} - \frac{3}{\hat{r}} \partial_{\hat{r}} p_{kl} - \frac{k^2}{\hat{r}^2} p_{kl} - \delta^2 (l\alpha)^2 p_{kl} = 0 \tag{2.16}$$

to the leading order where

$$\hat{p} = \sum_{k=0}^{\infty} \sum_{\substack{l=0 \\ l \text{ even}}}^{\infty} p_{kl}(\hat{r}) e^{il\alpha\tilde{z}} \cos(k\theta) + \sum_{k=0}^{\infty} \sum_{\substack{l=1 \\ l \text{ odd}}}^{\infty} p_{kl}(\hat{r}) e^{il\alpha\tilde{z}} \sin(k\theta). \tag{2.17}$$

Similar summation representations are available for $\hat{\mathbf{v}}_\perp$ and $\hat{w}$. For large $\hat{r}$ the functions p_{kl} above are such that

$$p_{kl}(\hat{r}) \sim \hat{D}_{k,l} \hat{r}^{\,2-\sqrt{k^2+4}} + C.C.\,, \tag{2.18}$$

for any axial Fourier-mode l. This implies that the k-azimuthal mode for $k \geqslant 2$ is such that

$$(u_k, v_k) \sim \hat{r}^{-\sqrt{k^2+4}-1}\, \hat{r} >> 1, \tag{2.19}$$

and using the continuity equation or divergence-free condition for the waves, the corresponding streamwise component becomes

$$w_k \sim \hat{r}^{-\sqrt{k^2+4}-2}. \tag{2.20}$$

The results (2.19)–(2.20) are valid for any $l \geqslant 1$, though the constants omitted in the $\sim$ relation can depend on l.

3. The computational scheme

We are interested in solving the nonlinear eigenvalue problem defined by equations (2.10) and (2.11) in a cylindrical pipe of infinite scaled radius subject to the regularity of the solution at $r = 0$ and the asymptotic far-field conditions (2.18)–(2.19). For computational simplicity we truncate the radial domain to $(0, L)$ with a value of L large enough to allow us to use the far-field matching at the boundary. Similar to the method described in Ozcakir *et al.* (2016) a Galerkin truncation of Fourier modes in θ and $\tilde{z} = z - ct$ and a collocation method with appropriately chosen radial basis functions in $\hat{r} \in (0, L)$ are used. The calculations described are limited to $k_0 = 2$; i.e. two-fold azimuthally symmetric TW states.

We write

$$\begin{pmatrix}\hat{u}\\ \hat{v}\\ \hat{w}\end{pmatrix} = \sum_{\substack{0\leqslant j\leqslant N\\ 0\leqslant k\leqslant M\\ 0\leqslant l \text{ even}\leqslant \mathrm{P}}} \begin{pmatrix}\left(u^{(1)}_{jkl}\cos l\alpha\tilde{z} + u^{(2)}_{jkl}\sin l\alpha\tilde{z}\right)\Phi_j(\hat{r};kk_0)\cos kk_0\theta\\ \left(v^{(1)}_{jkl}\cos l\alpha\tilde{z} + v^{(2)}_{jkl}\sin l\alpha\tilde{z}\right)\Phi_j(\hat{r};kk_0)\sin kk_0\theta\\ \left(w^{(1)}_{jkl}\sin l\alpha\tilde{z} + w^{(2)}_{jkl}\cos l\alpha\tilde{z}\right)\Psi_j(\hat{r};kk_0)\cos kk_0\theta\end{pmatrix} + \sum_{\substack{0\leqslant j\leqslant N\\ 0\leqslant k\leqslant M\\ 1\leqslant l \text{ odd}\leqslant \mathrm{P}}} \begin{pmatrix}\left(u^{(1)}_{jkl}\cos l\alpha\tilde{z} + u^{(2)}_{jkl}\sin l\alpha\tilde{z}\right)\Phi_j(\hat{r};kk_0)\sin kk_0\theta\\ \left(v^{(1)}_{jkl}\cos l\alpha\tilde{z} + v^{(2)}_{jkl}\sin l\alpha\tilde{z}\right)\Phi_j(\hat{r};kk_0)\cos kk_0\theta\\ \left(w^{(1)}_{jkl}\sin l\alpha\tilde{z} + w^{(2)}_{jkl}\cos l\alpha\tilde{z}\right)\Psi_j(\hat{r};kk_0)\sin kk_0\theta\end{pmatrix} \tag{3.1}$$

where Φ_j, Ψ_j are given in terms of Tchebyshev polynomials T_j as follows:

$$\Phi_j(\hat{r};k) = T_{2j}(\hat{r}/L) \text{ for } k \text{ odd } \Phi_j(\hat{r};k) = T_{2j+1}(\hat{r}/L) \text{ for } k \text{ even} \tag{3.2}$$

$$\Psi_j(\hat{r};k) = T_{2j+1}(\hat{r}/L) \text{ for } k \text{ odd } \Psi_j(\hat{r};k) = T_{2j}(\hat{r}/L) \text{ for } k \text{ even}. \tag{3.3}$$

Unlike the finite pipe flow problem, this basis does not satisfy outer boundary conditions. A Robin type boundary condition is imposed at $r = L$ consistent with the expected far-field behaviour of the rolls, streaks and waves discussed in section §2.2. For instance, the far-field scaling of the (k,l)'th Fourier mode $u_{kl}(\hat{r}) \sim \hat{r}^{\sigma_{kl}}$ for a given σ_{kl} leads to the following boundary condition at $\hat{r} = L$:

$$\hat{r}\frac{d}{dr}u_{kl}(\hat{r}) - \sigma_{kl}u_{kl}(\hat{r}) = 0$$

evaluated at $\hat{r} = L$. On the other hand, the pressure is calculated using a Poisson equation obtained by taking the sum $\nabla_\perp \cdot$ (2.10) + $\frac{\partial}{\partial\tilde{z}}$(2.11) and using the divergence condition (2.9). The following basis representation is used for the pressure:

$$\hat{p} = \sum_{\substack{0\leqslant j\leqslant N\\ 0\leqslant k\leqslant M\\ 0\leqslant l \text{ even}\leqslant \mathrm{P}}} \left(p^{(1)}_{jkl}\cos l\alpha\tilde{z} + p^{(2)}_{jkl}\sin l\alpha\tilde{z}\right)\phi_j(\hat{r};kk_0)\cos kk_0\theta + \sum_{\substack{0\leqslant j\leqslant N\\ 0\leqslant k\leqslant M\\ 1\leqslant l \text{ odd}\leqslant \mathrm{P}}} \left(p^{(1)}_{jkl}\cos l\alpha\tilde{z} + p^{(2)}_{jkl}\sin l\alpha\tilde{z}\right)\phi_j(\hat{r};kk_0)\sin kk_0\theta \tag{3.4}$$

where $\phi_j(\hat{r};0) = T_{2j+2}(\hat{r}/L)$, $\phi_j(\hat{r};k) = T_{2j+1}(\hat{r}/L)$ for k odd and $\phi_j(\hat{r};k) = T_{2j}(\hat{r}/L)$ for even.

Notice that the radial basis function $\phi_j(\hat{r};k)$ for $k = 0$ is chosen so that the pressure does not include a term with only a $\tilde{z}$-dependence. This is because, the Poisson equation remains unchanged after an addition of a function of $\tilde{z}$ to the pressure p, therefore the pressure is invariant up to an additive function $q(\tilde{z})$, which is taken care of by $H'(\tilde{z})$ in (2.11) so we can take that function to be zero in (3.4). The

solution $C2$ calculated from the full Navier–Stokes equations at a finite but large value of L is chosen as an initial guess in the Newton iteration scheme. The original solution that was defined on the radial domain $r \in (0, 1)$ is rescaled in terms of the new variable $\hat{r} \in (0, Re^{1/4})$ using (2.5) and (2.6). We then cut off the tail part $(L_0, Re^{1/4})$ at a suitable value of $L_0 < L < Re^{1/4}$ where each velocity component roughly exhibits an algebraic decay far from the core. Finally, the initial guess for the velocity profile is defined on the computational domain $\hat{r} \in (0, L)$ using the rescaled solution on $(0, L_0)$ and extrapolating it for (L_0, L) using the asymptotic scalings of the rolls, streaks and waves given in Section § 2.2.

4. Numerical results

4.1 *Comparison of the canonical solution and full numerical solution at finite Re*

The solution $(\hat{\mathbf{v}}_\perp, \hat{w}, c_1)$ to the canonical equations (2.10) and (2.11) was computed using the approach described in the above section. In order to interpret our results it is convenient to write the velocity $(\hat{u}, \hat{v}, \hat{w})^T$ in a Fourier series form as follows:

$$(\hat{u}, \hat{v}, \hat{w}) = \sum_{k,l \in \mathbb{Z}^2} (u_{kl}(\hat{r}), v_{kl}(\hat{r}), w_{kl}(\hat{r})) e^{ikk_0\theta} e^{il\alpha\tilde{z}}.$$

This representation allows us to focus on the radial dependence of velocity field at a given Fourier mode for each (k, l). The calculations described here are limited to the case $k_0 = 2$, i.e. two-fold azimuthally symmetric TW states with an axial wave number $\alpha = 1.55$. We used the $C2$ solution at $Re = 1.0282 \times 10^5$ from Ozcakir *et al.* (2016) as an initial guess for the canonical solution where the calculations were performed in the domain $(0, L)$ with the boundary conditions satisfied at $L = 61.184$. Experimentation showed that this value of L is large enough to enforce the required asymptotic trends. In the figures, we used $(N, M, P) = (265, 16, 5)$ to calculate the canonical solution. Resolution checks suggested that the calculation for c was accurate to the second digit and the velocity was accurate to the third digit.

Figures 1, 2, 3, 4, 5 and 6 show the magnitude of the velocity profiles $\hat{u}$, $\hat{v}$, $\hat{w}$ respectively as functions of $\hat{r}$ (solid curve) for different k, l modes where each component is compared to the corresponding velocity obtained by rescaling the shift-and-rotate symmetric $C2$ solutions using (2.5) and (2.6) at two different values of Re. Dotted curves denote results for $Re = 0.24 \times 10^6$, dashed dotted curves represent the calculations at $Re = 5.24 \times 10^6$. Note that, due to the imposed symmetry, one half of the azimuthal modes are zero in the Fourier expansion for each axial mode; we only plot the non-zero components. We choose to present the solution only inside the core where $\hat{r} < 10$ since the rescaled exact coherent states and canonical solutions are found to be indistinguishable beyond $L = 10$ for most of the Fourier modes. For comparison solutions to equation (2.5) and (2.6) are denoted by $(\tilde{u}_{kl}, \tilde{v}_{kl}, \tilde{w}_{kl})$ for each azimuthal mode k and axial mode l.

Based on the NVC theory, we expect the rescaled finite Re calculation to approach the canonical solution as $Re \to \infty$. All figures apart from Fig. 5 that is discussed later show conclusively that this is indeed the case. For the $l = 0, 1$ axial modes of radial and azimuthal velocities Figs 1, 2, 3 and 4 show that after rescaling both the $Re = 0.24 \times 10^6$ and $Re = 5.24 \times 10^6$ calculations, denoted by a dotted curve and crosses respectively, give very good approximations to the canonical solution. In fact the latter is almost a perfect match, which implies that to graphical accuracy the finite Re calculation is indistinguishable from the asymptotic regime for $l = 1$. When $l = 2$, the $Re = 0.24 \times 10^6$ solutions represented by the dotted curve still remain significantly different from the asymptotic $Re = \infty$ state,

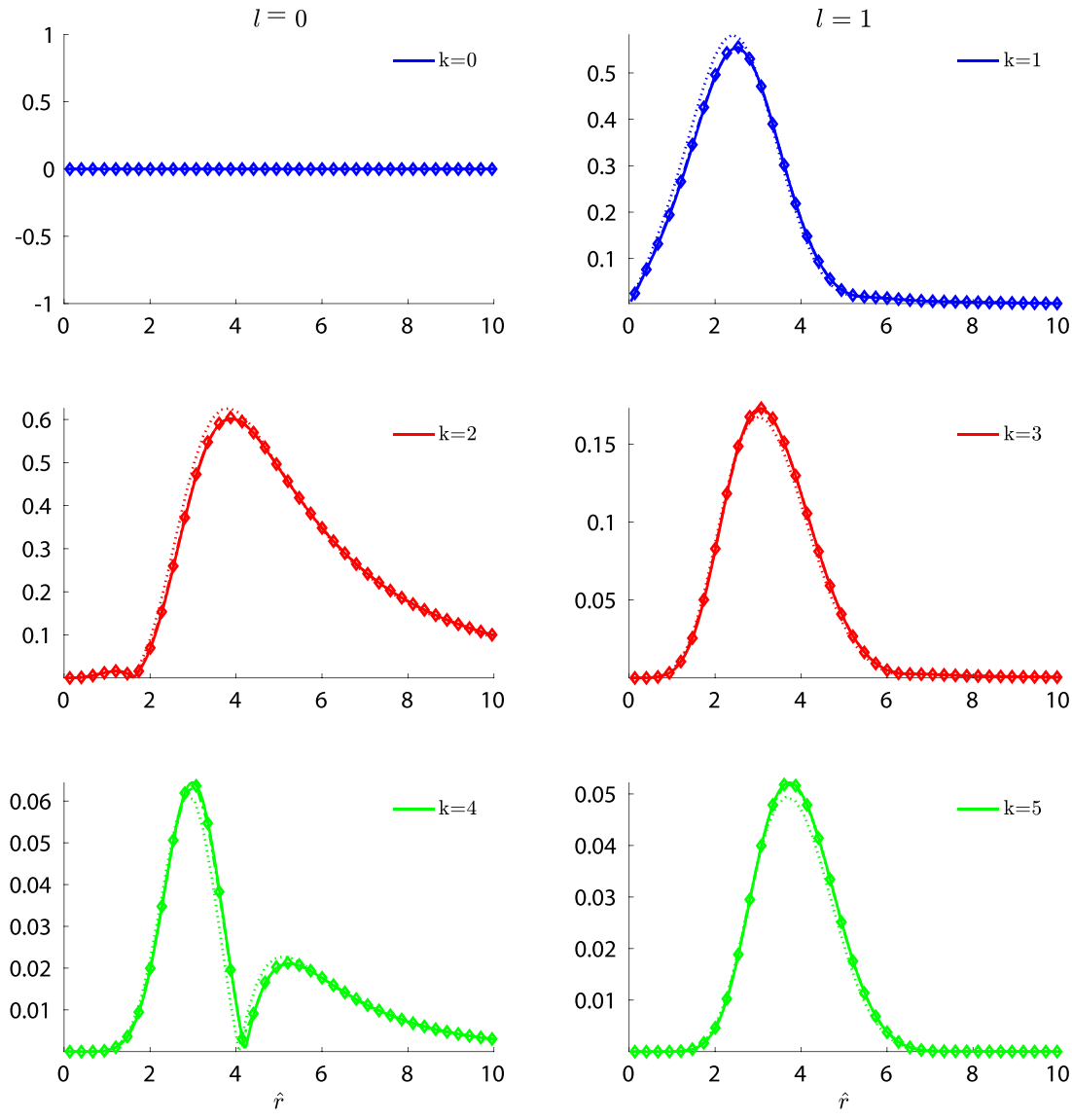

FIG. 1. The amplitude function $|u_{kl}(\hat{r})|$ of the k'th azimuthal, l'th axial Fourier modes of the radial components of the canonical NVC solution denoted by solid lines compared to the scaled amplitude function $Re^{3/4}|\tilde{u}_{kl}|$ of the radial components of the exact solutions of the full Navier–Stokes equations for $C2$ at $Re = 0.24 \times 10^6$ and $Re = 5.24 \times 10^6$, represented by dotted and dash-dotted lines, respectively, when $\alpha = 1.55$. Diamond markers are replaced by dash-dotted lines when those curves are indistinguishable from solid curves. The curves show the amplitudes as functions of $\hat{r} \in [0, 10]$ where $\hat{r} = Re^{1/4}r$. The first column shows the $l = 0$ axial modes (roll) for the non-zero azimuthal modes $k = 0, 2, 4$, while the $l = 1$ axial wave mode for the non-zero azimuthal modes $k = 1, 3, 5$ is given in the second column. Note that the continuity equation shows that the radial velocity is zero when $k = 0, l = 0$ but we show it for completeness.

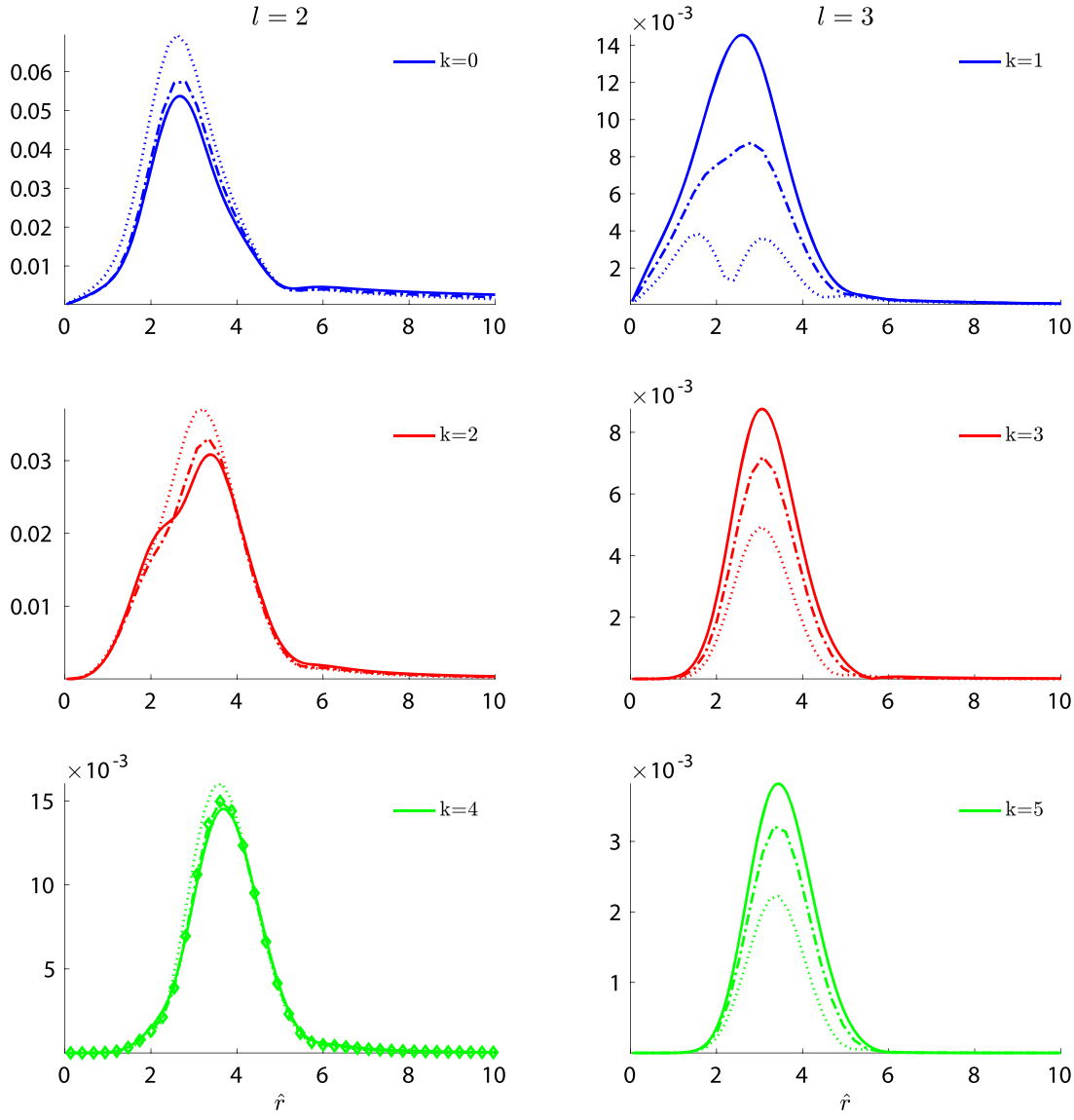

FIG. 2. The amplitude function $|u_{kl}(\hat{r})|$ of the k'th azimuthal, l'th axial Fourier modes of the radial components of the canonical NVC solution denoted by solid lines compared to the scaled amplitude function $Re^{3/4}|\tilde{u}_{kl}|$ of the radial components of the exact solutions of the full Navier–Stokes equations for $C2$ at $Re = 0.24 \times 10^6$ and $Re = 5.24 \times 10^6$, represented by dotted and dash-dotted lines, respectively, when $\alpha = 1.55$. Diamond markers are replaced by dash-dotted lines when those curves are indistinguishable from solid curves. The curves show the amplitudes as functions of $\hat{r} \in [0, 10]$ where $\hat{r} = Re^{1/4}r$. The first column shows the $l = 2$ axial modes (roll) for the non-zero azimuthal modes $k = 0, 2, 4$, while the $l = 3$ axial wave modes for the non-zero azimuthal modes $k = 1, 3, 5$ are given in the second column.

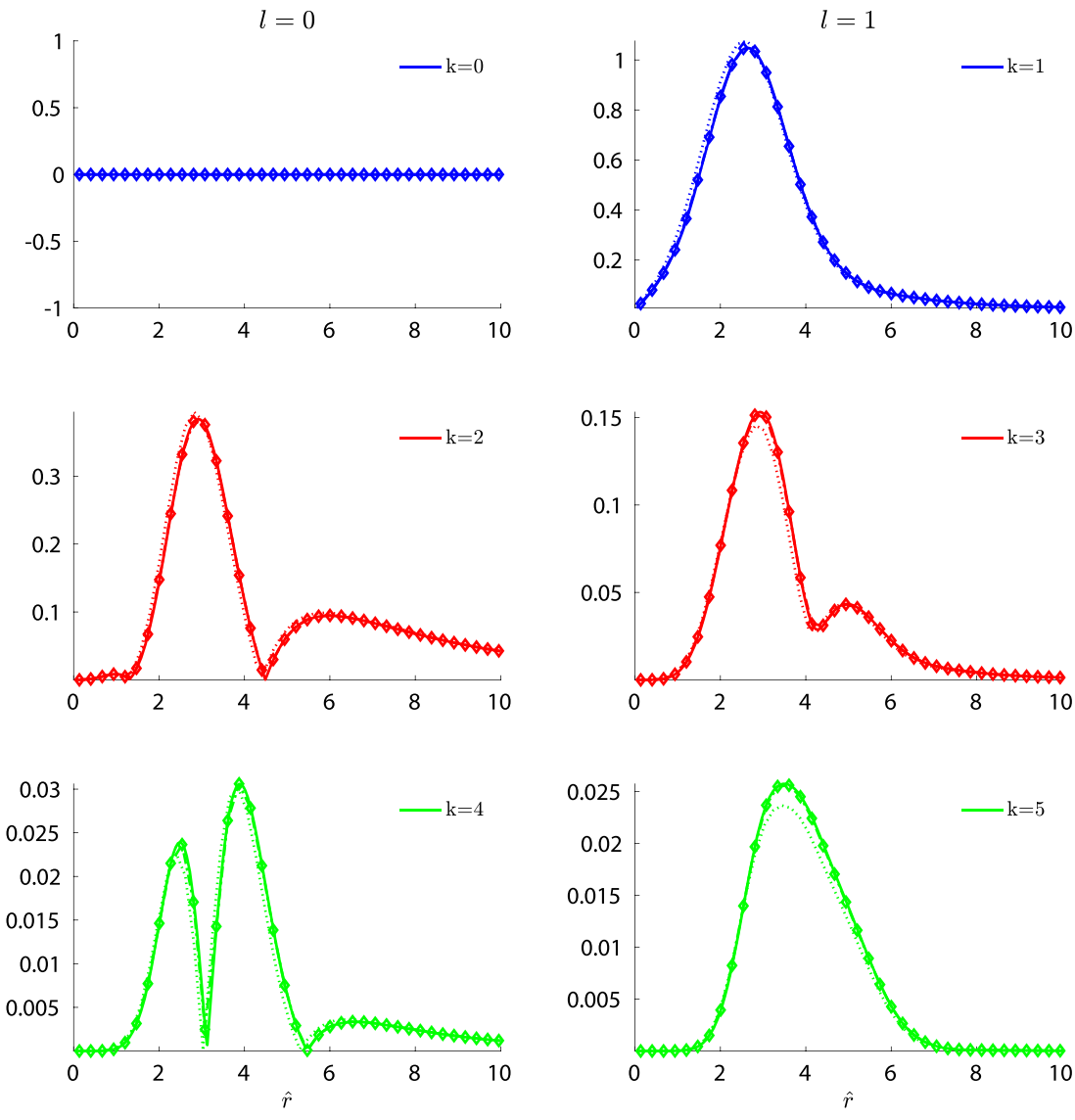

FIG. 3. The amplitude function $|v_{kl}(\hat{r})|$ of the k'th azimuthal, l'th axial Fourier modes of the azimuthal components of the canonical NVC solution denoted by solid lines compared to the scaled amplitude function $Re^{3/4}|\tilde{v}_{kl}|$ of the azimuthal components of the exact solutions of the full Navier–Stokes equations for $C2$ at $Re = 0.24 \times 10^6$ and $Re = 5.24 \times 10^6$, represented by dotted and dash-dotted lines, respectively, when $\alpha = 1.55$. Diamond markers are replaced by dash-dotted lines when those curves are indistinguishable from solid curves. The curves show the amplitudes as functions of $\hat{r} \in [0, 10]$ where $\hat{r} = Re^{1/4}r$. The first column shows the $l = 0$ axial modes (roll) for the non-zero azimuthal modes $k = 0, 2, 4$, while the $l = 1$ axial wave mode for the non-zero azimuthal modes $k = 1, 3, 5$ is given in the second column. The azimuthal velocity is zero when $k = 0$ due to the imposed shift-and-reflect symmetry, but is shown for completeness.

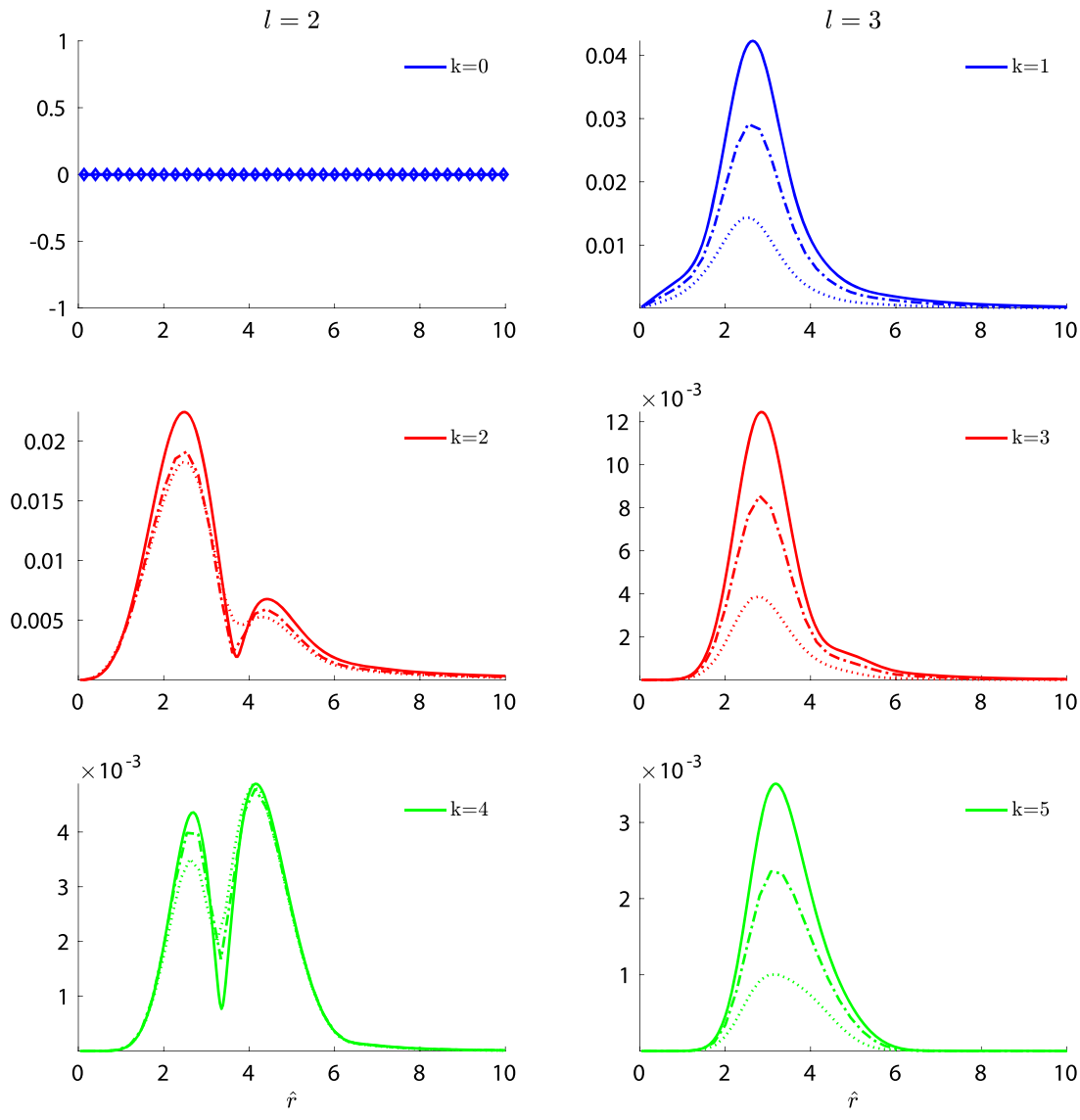

FIG. 4. The amplitude function $|v_{kl}(\hat{r})|$ of the k'th azimuthal, l'th axial Fourier modes of the azimuthal components of the canonical NVC solution denoted by solid lines compared to the scaled amplitude function $Re^{3/4}|\tilde{v}_{kl}|$ of the azimuthal components of the exact solutions of the full Navier–Stokes equations for $C2$ at $Re = 0.24 \times 10^6$ and $Re = 5.24 \times 10^6$, represented by dotted and dash-dotted lines, respectively, when $\alpha = 1.55$. Diamond markers are replaced by dash-dotted lines when those curves are indistinguishable from solid curves. The curves show the amplitudes as functions of $\hat{r} \in [0, 10]$ where $\hat{r} = Re^{1/4}r$. The first column shows the $l = 2$ axial modes (roll) for the non-zero azimuthal modes $k = 0, 2, 4$, while the $l = 3$ axial wave mode for the non-zero azimuthal modes $k = 1, 3, 5$ is given in the second column. The azimuthal velocity is zero when $k = 0$ due to the imposed shift-and-reflect symmetry but is shown for completeness.

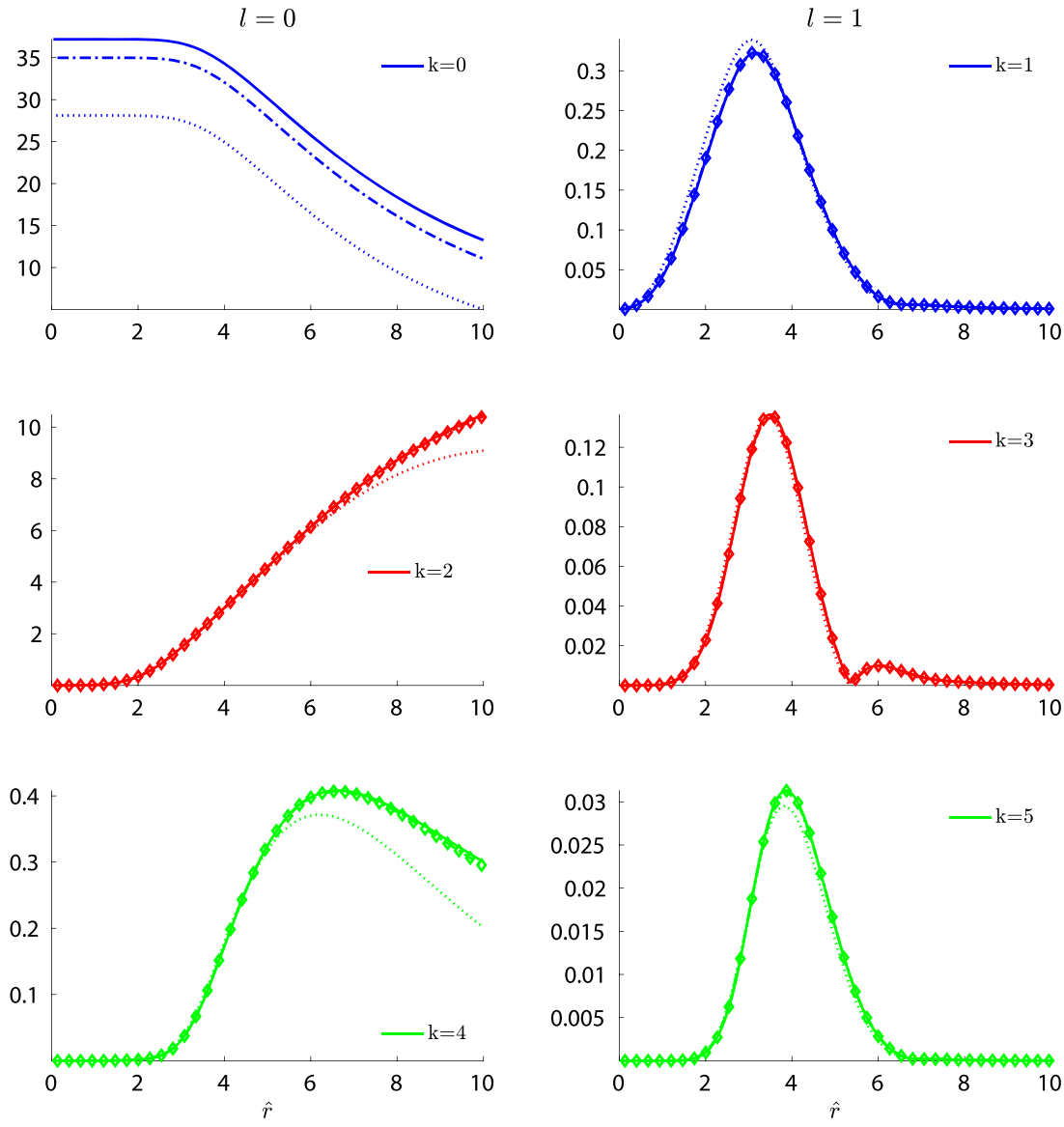

FIG. 5. The amplitude function $|w_{kl}(\hat{r})|$ of the k'th azimuthal, l'th axial Fourier modes of the axial components of the canonical NVC solution denoted by solid lines compared to the scaled amplitude function $Re^{1/2}|\tilde{w}_{kl}|$ of the axial components of the exact solutions of the full Navier–Stokes equations for $C2$ at $Re = 0.24 \times 10^6$ and $Re = 5.24 \times 10^6$, represented by dotted and dash-dotted lines, respectively, when $\alpha = 1.55$. Diamond markers are replaced by dash-dotted lines when those curves are indistinguishable from solid curves. The curves show the amplitudes as functions of $\hat{r} \in [0, 10]$ where $\hat{r} = Re^{1/4}r$. The first column shows the $l = 0$ axial modes (roll) for the non-zero azimuthal modes $k = 0, 2, 4$, while the $l = 1$ axial wave mode for the non-zero azimuthal modes $k = 1, 3, 5$ is given in the second column.

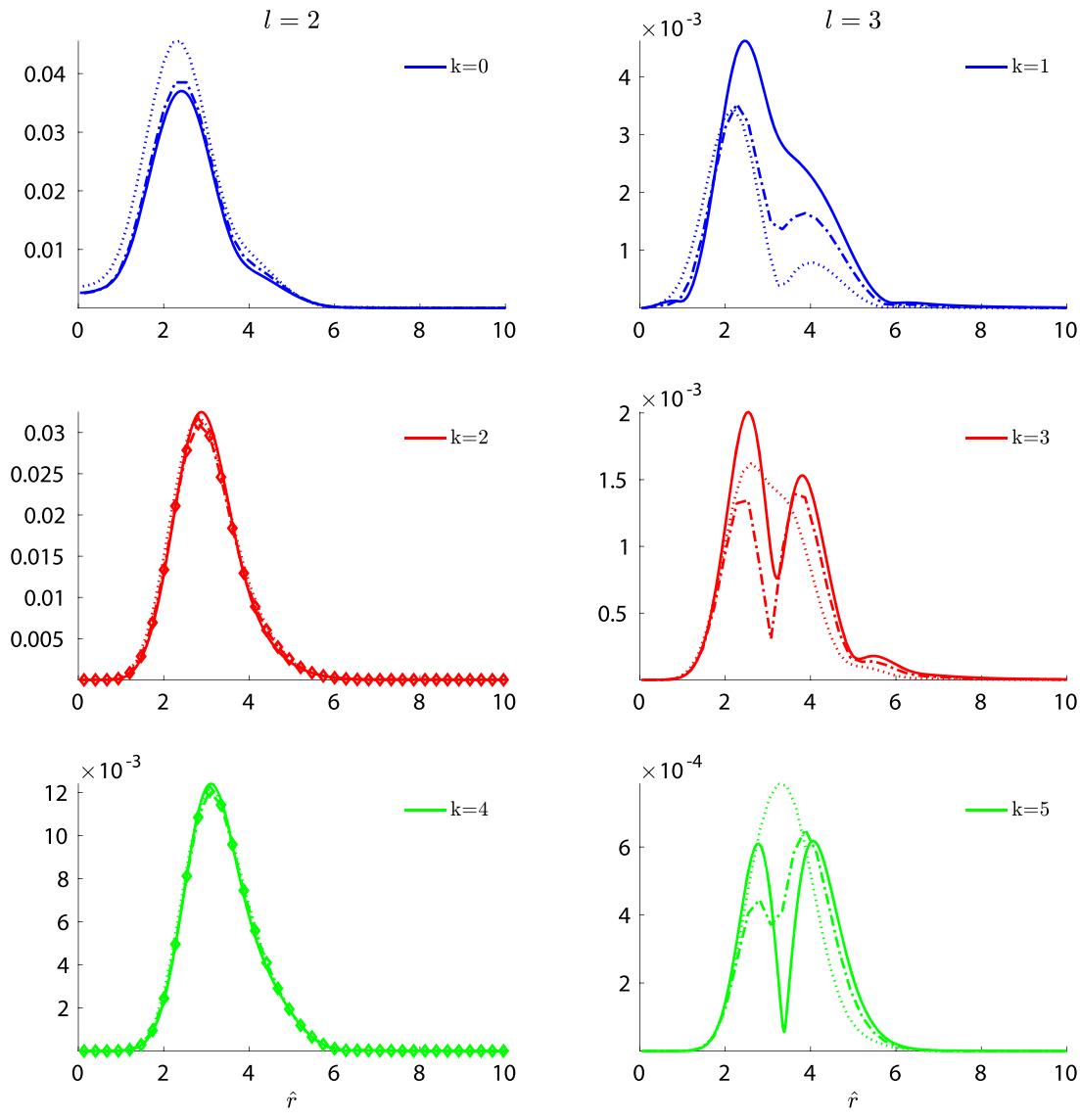

FIG. 6. The amplitude function $|w_{kl}(\hat{r})|$ of the k'th azimuthal, l'th axial Fourier modes of the axial components of the canonical NVC solution denoted by solid lines compared to the scaled amplitude function $Re^{1/2}|\tilde{w}_{kl}(r)|$ of the axial components of the exact solutions of the full Navier–Stokes equations for $C2$ at $Re = 0.24 \times 10^6$ and $Re = 5.24 \times 10^6$, represented by dotted and dash-dotted lines, respectively, when $\alpha = 1.55$. Diamond markers are replaced by dash-dotted lines when those curves are indistinguishable from solid curves. The curves show the amplitudes as functions of $\hat{r} \in [0, 10]$ where $\hat{r} = Re^{1/4}r$. The first column shows the $l = 2$ axial modes for non-zero azimuthal modes $k = 0, 2, 4$, while the $l = 3$ axial wave mode for the non-zero azimuthal modes $k = 1, 3, 5$ is given in the second column.

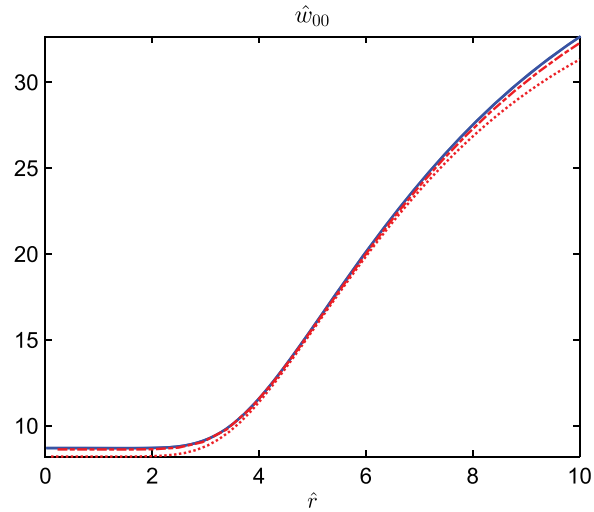

FIG. 7. The function $\langle\hat{w}\rangle + c_1$ for the NVC solution (solid), $Re^{1/2}\langle w\rangle$ component of the scaled exact solution $C2$ at $Re = 0.24\times10^6$ (dotted), $Re = 5.24 \times 10^6$ (dashed dot) where $\hat{r} = Re^{1/4}r$ as a function of $\hat{r} \in [0, 10]$.

though increasing Re to $Re = 5.24 \times 10^6$ brings the solutions in closer agreement with the canonical solutions. For $l = 3$, the finite Re calculations are clearly much further from the asymptotic regime; this is not unexpected since the effective Re is smaller for the modes with larger k or l. This implies that Re has to be much larger than the value of those used in our finite Re calculations to get close to the asymptotically predicted profile when k or l get progressively higher. Another reason for the poor agreement for the $l = 3$ modes is that any computational error for waves at finite but a large Re is amplified by the scaling factor proportional to $Re^{3/4}$ or $Re^{1/2}$, for the axial or non-axial modes, respectively. These modes are small in magnitude relative to the $l = 1$ components and therefore have larger relative errors. Therefore, rescaling these numerically less resolved higher axial modes with a very large Reynolds number will amplify the numerical error that will result in a much larger absolute error.

The axial velocity components in Figs 5 and 6 show similar results except for the case $l = 0$, which describes the behaviour of the streaks. The rescaled $C2$ mean flow approaches the canonical state as Re gets larger; however it is still far from the asymptotic limit. This is because the distinction between c_1 and the azimuthally averaged mean streak velocity $\langle\hat{w}\rangle$[1] only occurs in the boundary conditions rather than the equations (2.10) and (2.11). The differential equation only involves $c_1 + \langle\hat{w}\rangle$ and not c_1 and $\langle\hat{w}\rangle$ separately; it is only in the imposition of the far-field boundary condition that $\langle\hat{w}\rangle$ is distinguishable from c_1, and we believe this weak coupling explains the sizeable difference in the average streak component calculation between the finite Re calculation and the canonical solution. Indeed, when we compare $c_1 + \langle\hat{w}\rangle$ for the canonical solution with $Re^{1/2}(1 - c + \langle w\rangle)$ for finite but large Re, the agreement is much closer as shown in Fig. 7.

[1] Here $\langle\cdot\rangle$ notation denotes cross-sectional average

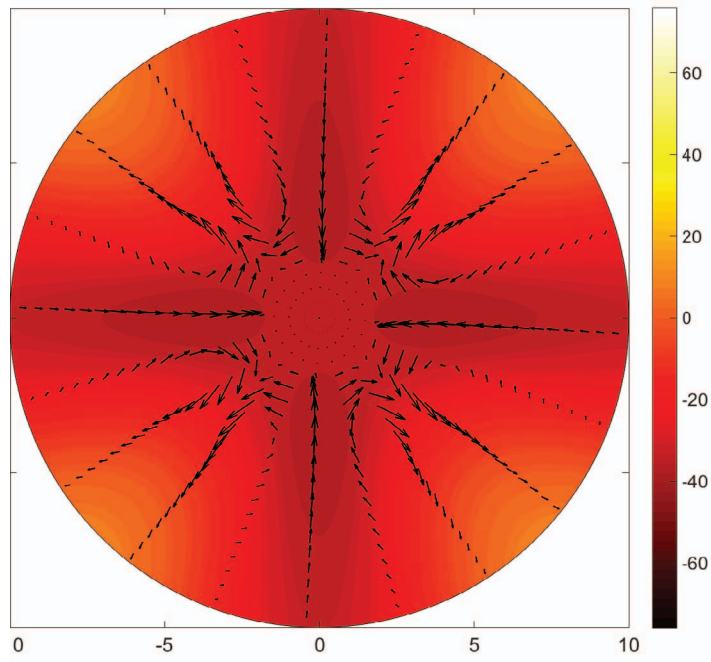

FIG. 8. The roll $(\mathbf{U}(r,\theta),\mathbf{V}(r,\theta))$ and streak $W(r,\theta)$ profile of the canonical solution for $\hat{r} \in [0, 10]$.

For the calculated canonical state, the streamwise averaged flows are displayed in a plane perpendicular to the pipe axis at several values of Re in Fig. 8, where the rolls (U, V) are depicted using arrows while the streak velocity intensity is represented in colours. The lighter orange colour corresponds to positive values of the streak velocity W, while the darker red colours correspond to negative values of W. The domain is restricted to the core of the pipe of infinite length where $\hat{r} \in [0, 10]$.

The visualization of the surfaces of constant magnitude of the velocity components $(\hat{u}, \hat{v}, \hat{w})$ of the canonical solution is shown in Fig. 9. The region inside the dark grey surface is where the streamwise velocity excluding the Poiseuille part is at least 90% of its maximum, while the blue/red coloured surfaces denote the region inside which the vorticity is at least 90% of its maximum/minimum for $\alpha = 1.55$ displayed in the interval $\hat{r} = [0, 10]$.

5. Conclusion

The work presented complements and completes the results presented in Ozcakir *et al.* (2016) where asymptotic scaling arguments were used to deduce a single parameter-free nonlinear system for the NVC type of exact coherent structures in the $Re = \infty$ asymptotic limit. This equation describes the fluid behaviour in the core around the pipe centre and it is supplemented with the far-field matching conditions when $\hat{r}$ is large. Here, we have presented numerical evidence for the existence of the solution postulated in the previous paper. Furthermore, for the purpose of comparison, we report direct numerical calculations of NVC states at much higher values of Re than previously reported.

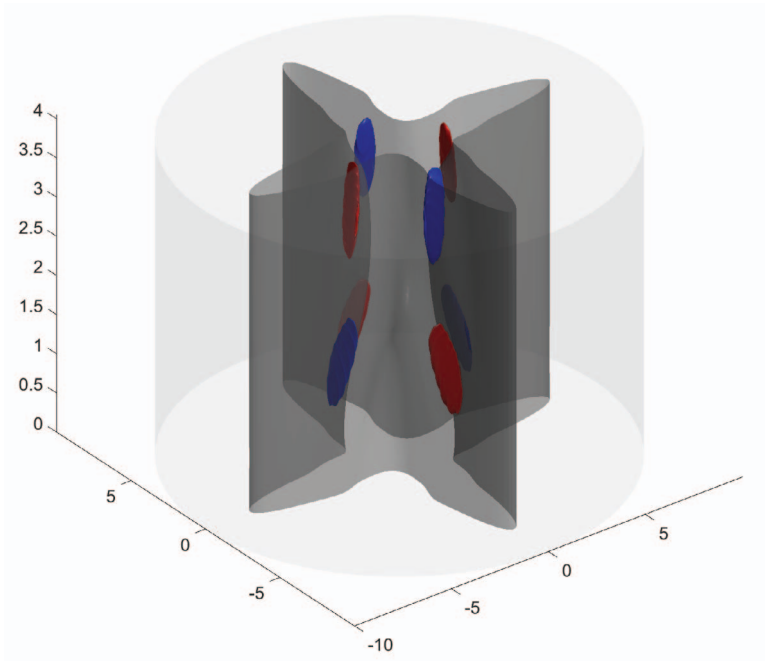

FIG. 9. The streamwise velocity and vorticity isosurfaces at a value 0.9 times of the values of the canonical solution for $\hat{r} \in [0, 10]$ for $\alpha = 1.55$.

We have shown that, apart from the streamwise and azimuthally averaged streamwise velocity, the solution to the canonical equation compares well with the full Navier–Stokes calculation for $Re = 5.26 \times 10^6$, and indeed agreement is excellent at significantly lower values of Re. The streamwise and azimuthally averaged streamwise velocity was seen to converge at a much slower rate to the canonical solution. The solution of the $Re = \infty$ asymptotic states obviates the need for continually calculating the NVC states at a sequence of larger and larger Reynolds number that is, in any case, not possible due to computational limitations.

These canonical states are reminiscent of the so-called free-stream coherent structure canonical states in the boundary layers (Deguchi & Hall, 2014b; Deguchi & Hall, 2014c; Deguchi & Hall, 2014d; Deguchi & Hall, 2018) except that in those cases the streak extends exponentially beyond the core region whereas the present calculations show that only one azimuthal component tends to a constant while the remaining modes decay algebraically.

Since the NVC state has a roll structure that collapses towards the pipe centre, it may be expected that similar states exist for pipe cross sections other than circular so long as the streamwise velocity of the unperturbed flow has a local maximum in the pipe's cross-section. The effect of the pipe cross-sectional shape shows up in the canonical equation in the far-field boundary conditions. In particular since the axial velocity instead of having a profile varying asymptotically like $\hat{r}^2$ in the far-field, it will generally asymptote to a profile of the form $Ax^2 + By^2$ for some positive A and B. This would necessarily break the four-fold symmetry of the streaks assumed here and will be the subject of future investigation. Nevertheless one expects that the NVC will exist in a modified form for any pipe flow with a local maximum of velocity.

Acknowledgements

This work made use of the facilities of National Computational Infrastructure (NCI), supported by the Australian Government under the project d77.

References

Blackburn, H.M., Hall, P. & Sherwin, S.J. (2013) Lower branch equilibria in Couette flow: the emergence of canonical states for arbitrary shear flows. *J. Fluid Mech.*, **726**, 12.

Smith, F. T. & Bodonyi, R. J. (1982) Amplitude-dependent neutral modes in the Hagen–Poiseille flow through a circular pipe. *Proc. R. Soc. Lond. A*, **384**, 463–489.

Smith, F. T., Doorly, D. J. & Rothmayer, A. P. (1990) On displacement-thickness, wall-layer and mid-flow scales in turbulent boundary layers, and slugs of vorticity in channel and pipe flows. *Proc. R. Soc. Lond. A*, **f428**, 255–281.

Deguchi, K. & Hall, P. (2014a) The high-Reynolds-number asymptotic development of nonlinear equilibrium states in plane Couette flow. *J. Fluid Mech.*, **750**, 99–112.

Deguchi, K. & Hall, P. (2014b) Free-stream coherent structures in parallel boundary-layer flows. *J. Fluid Mech.*, **752**, 602–625.

Deguchi, K. & Hall, P. (2014c) Canonical exact coherent structures embedded in high Reynolds number flows. *Phil. Trans. R. Soc*, **a 372**, 20130352.

Deguchi, K. & Hall, P. (2014d) Free-stream coherent structures in growing boundary-layers: a link to near-wall streaks. *J. Fluid Mech.*, **778**, 451–484.

Deguchi, K. & Hall, P. (2018) Free-stream coherent structures in a planar jet. *J. Fluid Mech.*, **837**, 916–930.

Deguchi, K. & Walton, A.G. (2013) A swirling spiral wave solution in pipe flow, *J. Fluid Mech*, **737**, 1–12.

Faisst, H. & Eckhardt, B. (2003) Traveling waves in pipe flow. *Phys. Rev. Lett.*, **91**, 224502.

Gibson, J. F., Halcrow, J. & Cvitanovic, P. (2009) Equilibrium and travelling-wave solutions of plane Couette flow. *J. Fluid Mech*, **638**, 243–266.

Hall, P. & Sherwin, S. (2010) Streamwise vortices in shear flows: harbingers of transition and the skeleton of coherent structures. *J. Fluid Mech.*, **661**, 178–205.

Hall, P. & Smith, F. (1991) On strongly nonlinear vortex/wave interactions in boundary layer transition. *J. Fluid Mech.*, **227**, 641–666.

Hof, B., van Doorne, C., Westerweel, J., Nieuwstadt, F., Faisst, H., Eckhardt, B., Wedin, H., Kerswell, R., & Waleffe, F. (2004) Experimental observation of nonlinear traveling waves in the turbulent pipe flow. *Science* **305**, 1594–1598.

Ozcakir, O., Tanveer, S., Hall, P. & Overman, E. A. (2016) Travelling waves in pipe flow. *J. Fluid Mech*, **791**, 284–328.

Ozcakir, O., Hall, P. &, Tanveer, S. (2019) Nonlinear exact coherent structures in pipe flow and their instabilities. *J. Fluid Mech*, **868**, 341–368.

Nagata, M. (1990) Three dimensional finite-amplitude solutions in plane Coutte flow: bifurcation from infinity. *J. Fluid Mech*, **217**, 519–527.

Pringle, C.C.T. & Kerswell, R.R. (2007) Asymmetric, helical and mirror-symmetric travelling waves in pipe flow. *Phys. Rev. Lett.*, **99**, 074502.

Viswanath, D. (2007) Recurrent motions within plane Couette turbulence. *J. Fluid Mech*, **580**, 339–358.

Viswanath, D. (2009) Critical layer in pipe flow at high Reynolds number. *Phi. Trans. R. Soc. A*, **580**, 561–576.

Viswanath, D. & Cvitanovic, P. (2009) Stable manifolds and the transition to turbulence in pipe flow. *J. Fluid Mech*, **627**, 215–233.

Waleffe, F. (1995) Hydrodynamic stability and turbulence: beyond transients to a self-sustaining process, *Stud. Appl. Math.* **95**, 319–343.

Waleffe, F. (2001) Exact coherent structures in channel flow. *J. Fluid Mech*, **435**, 93–102.

WALEFFE, F. (2003) Homotopy of exact coherent structures in plane shear flows. *Phys. Fluids*, **15**, 1517–1534.
WANG, J., GIBSON, J. & WALEFFE, F. (2007) Lower branch coherent states in shear flows: transition and control. *Phys. Rev. Lett.*, **98**, 204501.
WEDIN, H. & KERSWELL, R. (2004) Exact coherent structures in pipe flow: travelling wave solutions. *J. Fluid Mech*, **508**, 333–371.
WILLIS, A. P., DUGUET, Y., OMEL'CHENKO, O. & WOLFRUM, M. (2017) Surfing the edge: using feedback control to find nonlinear solutions. *J. Fluid Mech*, **831**, 579–591.